COMMUNICATIONS IN NUMERICAL METHODS IN ENGINEERING
Commun. Numer. Meth. Engng (2008)
Published online in Wiley InterScience (www.interscience.wiley.com). DOI: 10.1002/cnm.1202

A new numerical method for BLT forward problem based on high-order finite elements

Yanbin Hou[1], Jie Tian[1,2,*,†], Yan Wu[1], Jimin Liang[1] and Xiaowei He[1]

[1]*Life Science Research Center, School of Electronics Engineering, Xidian University, Xi'an 710071, Shaanxi, People's Republic of China*
[2]*Medical Image Processing Group, Institute of Automation, Chinese Academy of Sciences, Beijing 100080, People's Republic of China*

SUMMARY

Molecular imaging possesses the ability to characterize and measure biological processes at the cellular and molecular level *in vivo*. As one of the new molecular imaging modalities, bioluminescence tomography (BLT) is to reconstruct the light distribution inside a small animal from the photon flux measured on its surface. To obtain accurate and robust reconstruction, it needs a good understanding of the propagation of photons in biological tissues, which is referred to as the forward problem in BLT. Because the turbid media is high scattering and low absorption, the propagation process can be described by the steady diffusion equation. In this paper, an *hp-adaptivity* method for BLT forward problem is presented based on finite elements of high orders and moderate meshes by finite element method (FEM). Both numerical simulation and physical experiment are performed to evaluate the accuracy of solution and the efficiency of computation. The relevant results show that element order is more critical than mesh size to produce an accurate FEM solution efficiently. Copyright © 2008 John Wiley & Sons, Ltd.

Received 1 April 2008; Revised 20 October 2008; Accepted 22 October 2008

KEY WORDS: molecular imaging; bioluminescence tomography; forward problem; high-order finite elements; diffusion approximation

1. INTRODUCTION

Modern medical imaging has undergone structural and functional imaging techniques since the discovery of X-ray by Wilhelm Konrad Roentgen in 1895. The relevant equipments, such as CT,

---

[*] Correspondence to: Jie Tian, Medical Image Processing Group, Institute of Automation, Chinese Academy of Sciences, Beijing 100080, People's Republic of China.

[†] E-mail: tian@IEEE.org

Contract/grant sponsor: National Basic Research Program of China (NBRPC); contract/grant number: 2006CB705700
Contract/grant sponsor: Program for Cheung Kong Scholars and Innovative Research Team in University (PCSIRT); contract/grant number: IRT0645
Contract/grant sponsor: Chair Professors of Cheung Kong Scholars Programme
Contract/grant sponsor: Shaanxi Science and Technology Programming; contract/grant number: 2007K08-06

MRI, PET, SPECT, etc, have brought great innovation in the diagnosis and treatment of diseases. These medical equipments help medical staff to observe and measure the tissue lesions more clearly and accurately. However, most of them are only able to screen the advanced stages of diseases. With the advances in biomedical and genetic engineering, molecular imaging provides promising solutions to early diagnosis of disease, personalized treatment, drug development, gene study and so on [1–3]. Compared with other molecular imaging techniques, optical imaging has the advantages of nano–molar sensitivity, high spatial resolution, short imaging time, low cost and so on [4, 5]. Optical imaging modalities include optical coherent tomography, diffusion optical tomography, photoacoustic tomography, optical-PET, bioluminescence tomography (BLT) and fluorescence molecular tomography [6, 7]. BLT is to reconstruct the bioluminescent light sources inside an object from the optical signals measured at its boundary, and to provide real-time detection and quantitative measurement of tagged cells while keeping the small living animals intact. Although optical imaging can only detect the surface light, BLT fails to get the depth information of targets under test directly [8]. Multi-spectral and multi-modality method are recently developed to improve the performance of BLT [9–11].

Since biological tissues are turbid, bioluminescent photons undergo absorption, reflection, scattering and other optical behaviors. BLT employs the near infrared light to image *in vivo* because the lowest coefficient of absorption occurs within the range of 650–900 nm [3]. Light propagation in biological tissues can be depicted by Monte Carlo method (MC) based on repeated random sampling, or by radiative transfer equation (RTE) based on classic transport theory [6, 12–14]. But both methods are computationally expensive. In high-scattering and low-absorption biological tissues, RTE is simplified as the diffusion equation (DE) with appropriate boundary condition, which provides a quite accurate description of the imaging model [15]. BLT problems consist of forward problem and inverse problem. Forward problem is to find out the light distribution with given light sources and tissue parameters, whereas inverse problem is either to determine tissue optical properties or to retrieve inner light sources from boundary measurement [16]. Mathematically, forward problem is to solve a partial differential equation. The solution is difficult to obtain analytically in most practical cases. Many numerical methods, such as finite difference methods, finite element method (FEM), boundary element method, are widely adopted [17–21]. Owing to the efficient and flexible discretization techniques, FEM has become well established in biomedical optics [22].

In this paper, we investigate the effects of mesh size and element order on FEM solution and evaluate the accuracy and the convergence compared with analytical solution, MC simulation and experimental measurement. In the second section, BLT forward problem is formulated by DE and then analyzed via FEM. In the third section, numerical simulation and physical experiment are performed to evaluate the accuracy and the efficiency of FEM. In the final section, results and conclusions are discussed.

2. THEORY AND METHOD

2.1. *Transport theory and RTE*

In BLT, forward problem is to find the photon density in the biological tissue and the outgoing flux on its boundary. Photon transport in biological tissue can be described with RTE based on

DOI: 10.1002/cnm

transport theory [12, 19]

$$\frac{\partial L(r,\hat{s},t)/V}{\partial t} = -\hat{s}\cdot\nabla L(r,\hat{s},t)-(\mu_a+\mu_s)L(r,\hat{s},t)$$
$$+\mu_s\int_{4\pi} L(r,\hat{s}',t)P(\hat{s}'\cdot\hat{s})\,\mathrm{d}\hat{s}'+S(r,\hat{s},t)\quad \forall r\in\Omega \tag{1}$$

where $L(r,\hat{s},t)$ denotes radiance at position r at time t into direction $\hat{s}$ in the unit of $\mathrm{W mm^{-2} sr^{-1}}$, V the velocity of light in tissues, μ_a and μ_s are absorption and scattering coefficients, respectively, in mm^{-1}, Phase function $P(\hat{s}'\cdot\hat{s})$ represents the probability distribution of light with propagation direction $\hat{s}'$ scattered into the direction $\hat{s}$, $S(r,\hat{s},t)$ is the inner light source in $\mathrm{W mm^{-3} sr^{-1}}$.

2.2. *Diffusion approximation and boundary conditions*

The RTE is difficult to solve since there are six independent variables. The RTE is usually simplified by diffusion approximation for high-scattering and low-absorption medium ($\mu_a \ll \mu_s$), where the radiance $L(r,\hat{s},t)$ is expanded to the first order of spherical harmonics. Thus the RTE (1) can be reduced to the DE [16]

$$\nabla\cdot D(\nabla\Phi(r,t))-\mu_a\Phi(r,t)=\frac{\partial\Phi(r,t)/V}{\partial t}-S(r,t)\quad\forall r\in\Omega \tag{2}$$

where $\Phi(r,t)$ is the instantaneous photon flux density at time t in $\mathrm{W mm^{-2}}$, $D=1/(3(\mu_a+(1-g)\mu_s))$ the optical diffusion coefficient in mm and g the anisotropy parameter.

Let $S(r,t)=\delta(r,t)$ and Ω be an infinite homogeneous domain, we can get Green's function solution to the DE:

$$\Gamma(r,t)=V(4\pi DVt)^{-3/2}\exp[-r^2/(4DVt)-\mu_a Vt]\quad\forall r\in\Omega \tag{3}$$

For an arbitrary source, the solution to Equation (2) can be obtained by the following convolution:

$$\Phi(r,t)=\Gamma(r,t)*S(r,t)=\int_0^t\int_\Omega \Gamma(r-r',t-t')S(r',t')\,\mathrm{d}r'\mathrm{d}t' \tag{4}$$

If the measurement is carried out in an ideal environment without outer light interference, the boundary condition for Equation (2) can be expressed as [23]

$$\Phi(r,t)+2A(r;n,n')D(v\cdot\nabla\Phi(r,t))=0\quad\forall r\in\partial\Omega \tag{5}$$

where v is the unit outer normal on boundary, n and n' are the refractive indices of inner and outer medium, respectively, $A(r;n,n')$ can be approximated as

$$A(r;n,n')\approx(1+R(r))/(1-R(r)) \tag{6}$$

where n' is close to 1 when experiments are performed in air, $R(r)$ is a parameter governing the internal reflection on boundary $\partial\Omega$ [19]:

$$R(r)\approx-1.4399n^{-2}+0.7099n^{-1}+0.6681+0.0636n$$

According to Fick's law, the outgoing flux density measured on the boundary is [8]:

$$G(r,t)=-D(v\cdot\nabla\Phi(r,t))=\Phi(r,t)/(2A(r;n,n')) \tag{7}$$

DOI: 10.1002/cnm

In real experiments, the bioluminescent sources are usually provided by mixing different chemical solutions, which can release constant power during quite a long period. This means we usually deal with photon flux density independent of time. From Equations (2) and (5), we can get the steady-state form of DE and its boundary condition as follows:

$$\begin{aligned} -\nabla\cdot(D\nabla\Phi(r))+\mu_{\mathrm{a}}\Phi(r) &= S(r) \quad \forall r\in\Omega \\ \Phi(r)+2A(r;n,n')D(v\cdot\nabla\Phi(r)) &= 0 \quad \forall r\in\partial\Omega \end{aligned} \tag{8}$$

2.3. *Analytical solution to steady-state DE*

It is difficult to obtain an analytical solution to the DE in most practical cases. However, when the model is simple, for example, infinite homogeneous medium enclosing a spherical source, the analytical solution can be calculated through Equation (4). The power density of a uniform spherical solid source in a three-dimensional spherical coordinate system can be written as [16, 24]

$$S(r,\theta,\phi)=\begin{cases} p & \text{for } 0\leqslant\theta\leqslant 2\pi,\ 0\leqslant\phi\leqslant\pi,\ 0\leqslant r\leqslant r_0 \\ 0 & \text{else} \end{cases} \tag{9}$$

where p is the light source power in W, r_0 is the radius of the spherical source in mm, θ denotes the polar angle and ϕ the azimuthal angle.

Substituting Equation (9) into Equation (4) and simplifying the convolution, we can derive the analytical solution to the steady-state DE [24]:

$$\Phi(r)=\frac{p\exp[-\mu_{\mathrm{eff}}r]}{rD(\mu_{\mathrm{eff}})^2}\left(r_0\cosh(\mu_{\mathrm{eff}}r_0)-\frac{1}{\mu_{\mathrm{eff}}}\sinh(\mu_{\mathrm{eff}}r_0)\right) \tag{10}$$

where r_0 denotes the radius of the spherical source, r denotes the distance between the source surface and measuring point, μ_{eff} is the effective attenuation coefficient defined as $\mu_{\mathrm{eff}}=\sqrt{\mu_{\mathrm{a}}/D}$.

2.4. *Weak form and FEM formulation*

The weak form of Equation (8) is to find $\Phi(r)$ such that

$$\int_{\Omega} D\nabla\Phi(r)\cdot\nabla\Psi(r)\,\mathrm{d}r+\int_{\Omega}\mu_{\mathrm{a}}\Phi(r)\Psi(r)\,\mathrm{d}r+\int_{\partial\Omega}\frac{1}{2A}\Phi(r)\Psi(r)\,\mathrm{d}r=\int_{\Omega}S(r)\Psi(r)\,\mathrm{d}r \tag{11}$$

where $\Psi(r)$ is an arbitrary piecewise continuous test function [23]. According to the standard finite element analysis, domain Ω is decomposed into T vertex nodes $(N_1, N_2, \ldots, N_T)$ and N_e mesh elements, denoted as e_l $(l=1,2,\ldots,N_e)$. Let the set $E=\{e_l\}$ be triangulation. Then $\Phi(r)$ can be expressed approximately as

$$\Phi(r)\approx\Phi^h(r)=\sum_{k=1}^{T}\phi_k\varphi_k(r) \quad \forall r\in\Omega \tag{12}$$

where ϕ_k is the approximate nodal value of $\Phi(r)$ on the node N_k, $\varphi_k(r)$ is the nodal basis function with support over the elements e_l, which have the node N_k as a common vertex. In the same way, the source is approximated as

$$S(r)\approx S^h(r)=\sum_{k=1}^{Ts}s_k\gamma_k(r) \quad \forall r\in\Omega \tag{13}$$

where $\{s_k\}$ is the interpolation node values of $S(r)$ and $\gamma_k(r)$ the interpolation basis functions, which may be the same with or different from $\varphi_k(r), Ts$ is the number of interpolation basis functions. Usually, tissue consists of several organs and Ts is much smaller than T. We adopt a global node numbering scheme for each organ and light source to deal with the discontinuities in optical coefficients. Using $\varphi_k(r)$ as the test function and substituting Equations (12) and (13) into Equation (11), we have:

$$\sum_{i,j}\left\{\int_\Omega D\nabla\varphi_i\cdot\nabla\varphi_j\,\mathrm{d}r+\int_\Omega \mu_\mathrm{a}\varphi_i\varphi_j\,\mathrm{d}r+\int_{\partial\Omega}\frac{1}{2A}\varphi_i\varphi_j\,\mathrm{d}r\right\}\phi_i=\sum_{i,j}\left\{\int_\Omega \gamma_i\varphi_j\,\mathrm{d}r\right\}s_i \tag{14}$$

By defining the system matrix $M=(M_{ij})\in R^{T\times T}$ and the vector $F=(f_i)\in R^{T\times 1}$:

$$M_{ij}=\int_\Omega D\nabla\varphi_i\cdot\nabla\varphi_j\,\mathrm{d}r+\int_\Omega \mu_\mathrm{a}\varphi_i\varphi_j\,\mathrm{d}r+\int_{\partial\Omega}\frac{1}{2A}\varphi_i\varphi_j\,\mathrm{d}r$$

$$f_i=\sum_j\left\{\int_\Omega \gamma_i\varphi_j\,\mathrm{d}r\right\}s_i$$

Equation (14) becomes a linear equation as follows:

$$M\phi=F \tag{15}$$

where $\phi=(\phi_i)$, $i=1,2,\ldots,N_e$. M is a sparse, symmetric and positive-definite system matrix. Hence, the solution to Equation (8) is to find out a series of nodal values of $\Phi(r)$.

As a linear equation, Equation (15) is generally solved by direct solvers or iterative solvers. The formers introduce matrix factorization and Gauss elimination, while the latters need initial values and proper preconditioners to accelerate the convergence.

2.5. High-order basis functions

As was mentioned above, domain under investigation is partitioned into a set of mesh elements. These finite elements are of simple shapes, such as triangle, quadrilateral for 2D domain and tetrahedron, prism for 3D domain. Since triangular elements have better approximation of irregular geometry, we employ tetrahedral elements for subdomains and triangular elements for the boundary.

After the discretization of domain Ω into finite elements, approximations to the dependent variables need to be introduced, as illustrated in Equation (12). That means one should approximate $\Phi(r)$ with a function $\Phi^h(r)$ in finite element spaces. ϕ_k is called *degrees of freedom* (DOFs), and $\varphi_k(r)$ the nodal basis function. In terms of the finite element, basis function can be linear, quadratic, cubic or even higher order [25, 26]. In this paper, we construct piecewise continuous basis functions by using Lagrange interpolation.

For 1D domain, $\Phi(x)$, which passes through $n+1$ points (x_0,y_0), $(x_1,y_1),\ldots,(x_n,y_n)$, is a linear combination of Lagrange interpolation basis functions:

$$\begin{aligned}\Phi(x)&=\sum_{k=0}^{n}y_kN_k(x)\\ N_k(x)&:=\prod_{\substack{j=0\\ j\neq k}}^{n}\frac{(x-x_j)}{(x_k-x_j)}\end{aligned} \tag{16}$$

DOI: 10.1002/cnm

It is obvious that 1D Lagrange basis functions satisfy following properties [27]:

(1) $0 \leqslant N_k(x) \leqslant 1$.
(2) $N_k(x_j) = \delta_{jk}$.
(3) $\sum_k N_k(x) = 1$.

According to the definition in Equation (16), $\varphi_k(x)$ is of degree at most $n-1$. The more points that are used in the interpolation, the higher the degree of the basis function, as shown in Figure 1.

For 2D domain, the description of basis functions is simplified by the introduction of *barycentric coordinates* [28] for simplicity. In the context of triangle, barycentric coordinates are also known as area coordinates. As illustrated in Figure 2, coordinates of P with respect to triangle ABC are proportional to the areas of PBC, PCA and PAB.

If we define:

$$L_1 = \frac{S_{\Delta PBC}}{S_{\Delta ABC}}, \quad L_2 = \frac{S_{\Delta PCA}}{S_{\Delta ABC}}, \quad L_3 = \frac{S_{\Delta PAB}}{S_{\Delta ABC}} \tag{17}$$

The area coordinates (L_1, L_2, L_3) of vertices A, B and C are $(1,0,0), (0,1,0)$ and $(0,0,1)$, respectively. Obviously, L_1, L_2 and L_3 satisfy properties (1), (2) and (3). Thus we can express

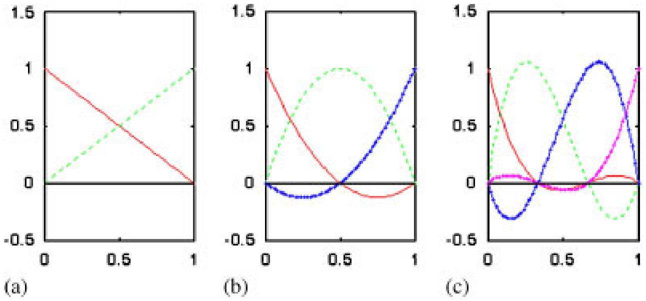

Figure 1. 1D Lagrange interpolation basis function: (a) linear; (b) quadratic; and (c) cubic.

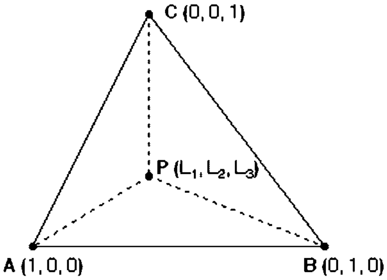

Figure 2. Triangular area coordinates for linear basis function.

DOI: 10.1002/cnm

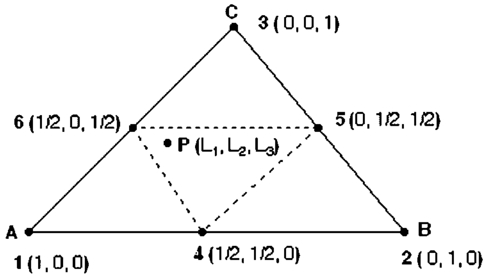

Figure 3. Triangular area coordinates for quadratic basis function.

$\Phi(r)$ as a combination of linear Lagrange interpolation basis functions

$$\Phi(r)=\sum_{k=1}^{3}\phi_k\varphi_k(r) \quad \forall r\in\Delta P_i P_j P_m \tag{18}$$

where $\varphi_k=L_k, k = 1, 2, 3$.

Because area coordinates do not depend neither on the shape nor on the position of the triangular finite element, it is quite convenient to derive the quadratic and cubic Lagrange interpolation basis functions

$$\varphi_k=\prod_{j=1}^{m}\frac{f_j^{(k)}(L_1,L_2,L_3)}{f_j^{(k)}(L_{1k},L_{2k},L_{3k})}, \quad k=1,2,\ldots,N \tag{19}$$

where m is the degree of $\varphi_k, f_j^{(k)}(L_1,L_2,L_3)$ is the left-hand side of straight-line equation excluding the kth node, $f_j^{(k)}(L_{1k},L_{2k},L_{3k})$ the area coordinates on the kth node, $N=(m+1)(m+2)/2$ the number of nodes contained in the triangular element.

Based on Equation (19), it needs to add other three nodes to build quadratic basis function, as shown in Figure 3. Nodes 4 to 6 are the midpoints of three edges, and $\Phi(r)$ is expressed as follows:

$$\Phi(r)=\sum_{k=1}^{6}\phi_k\varphi_k(r) \quad \forall r\in\Delta ABC \tag{20}$$

where $\varphi_k=L_k(2L_k-1)$, $k=1,2,3$, $\varphi_4=4L_2L_3$, $\varphi_5=4L_3L_1$, $\varphi_6=4L_1L_2$.

Likewise, the basis functions of different orders for 3D can be constructed by the introduction of volume coordinates. In general, basis function of high order specifies a finite element space with better accuracy while the drawback is that DOFs increase.

2.6. *Error estimation and convergence*

FEM formulation is the discretization of the original problem, the error between exact solution and approximation is bounded by [29]

$$\|\Phi-\Phi^h\|\leqslant Ch^{\min(m-1,p)} \tag{21}$$

DOI: 10.1002/cnm

where $\|\cdot\|$ denotes the Euclidean norm, h is the maximum mesh size, p is the degree of the basis function and m is a measure of the order of the singularity in the problem. In order to reduce the error, three versions of FEM may be adopted, which correspond to shortening the element size by *h-adaptivity*, increasing the degree of basis function by *p-adaptivity* and swapping the edge and facet of the element by *r-adaptivity*, respectively.

In theory, if the maximum mesh size is sufficiently small, the numerical solution to Equation (15) could converge to the exact solution of Equation (8) [23]. But the smaller h is, the more unknowns in Equation (15), need to be found out. In practice, we usually have to make a tradeoff between the solution accuracy and computation overhead. In this paper, h-p FEM is applied, where convergence can be achieved by refining mesh element or by increasing the approximation order or by a combination of both [30]. Convergence order n is evaluated by:

$$n=\frac{\ln\|\Phi-\Phi^h\|-\ln(c)}{\ln(h)}, \quad c\in(0,1] \tag{22}$$

In the next section, we will study the effects of h and p on the accuracy and the convergence of FEM solutions with numerical simulation and physical experiment.

3. SIMULATION AND EXPERIMENT

In study of BLT forward problem by FEM, the domain under consideration is first described by creating geometry. Second, the region of interest (ROI) is discretized into finite elements by meshing, and then through assigning relevant parameters and selecting appropriate basis functions we form a group of linear equations as described in Section 2. Finally, a proper solver is employed and the unknown variables are determined. Extensive comparisons were made to evaluate the effects of high-order FEM on the accuracy of solution and the efficiency of computation. In our simulations, we partitioned the geometric model into tetrahedral elements with Netgen 4.3, and the main computational platform is a Compaq desktop computer, dc7700 with Intel Core$^{\text{TM}}$ 2 CPU 6300 @ 1.86 GHz and 2 GB RAM.

3.1. Comparison with analytical solution

3.1.1. The accuracy of FEM solution. In order to examine the accuracy compared with the analytical solution obtained by Equation (10), we adopted the homogeneous phantom from Hui [16]. As shown in Figure 4(a), the phantom consists of concentric spheres. The inner ball of the radius 0.3 mm was a solid uniform light source with power of 1 μW. The outer was the tissue with optical parameters of $\mu a=0.082\,\text{mm}^{-1}$, $\mu s=10.27\,\text{mm}^{-1}$, $g=0.90$ and $n=1.37$. Figure 4(b) shows the phantom mesh after discretization with a radius of 4 mm and moderate mesh size. With radius of tissues varying from 2 to 10 mm, we obtained a group of flux density values. Because the solutions to Equation (15) were the nodal values of $\Phi(r)$ on overall nodes, whereas the solution to Equation (10) was a point value on the phantom surface, some work must be done as a necessary preprocessing step. Here, we integrated solutions over the tissue surface to derive the photon flux in Watt.

As it was expected, both results from FEM and analytical formula declines with the increasing radius of phantom surface, as shown in Figure 5. The numerical solutions show good accordance with the analytical solutions.

DOI: 10.1002/cnm

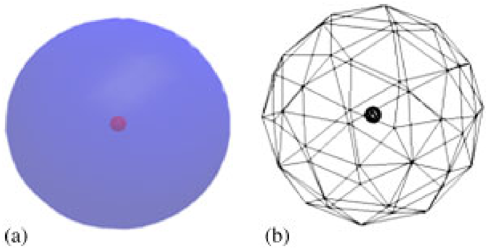

Figure 4. Spherical homogenous phantom containing a solid ball source: (a) geometric model and (b) mesh elements after moderate discretization.

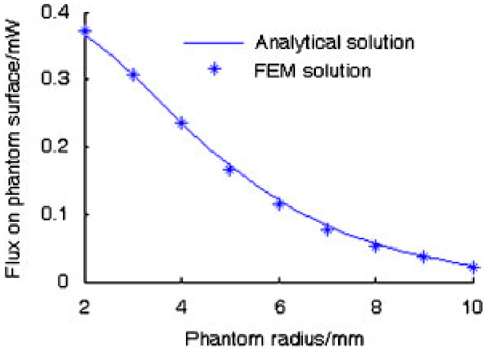

Figure 5. Comparison between FEM solution and analytical solution.

3.1.2. The convergence of high-order elements. We constructed basis functions by Lagrange interpolation in this paper. The basis function is a piecewise continuous on each element and its degree is equal to the order of the Lagrange element. The higher the order is, the smoother the basis function is, and the better the numerical solution approaches the true solution [15, 24]. Three groups of FEM solutions were obtained by adopting tetrahedral elements of different orders, all the geometric and optical parameters were the same as those in Section 3.1.1 except that the tissue was fixed with a radius of 4 mm. Figure 6 demonstrates the comparison, and Tables I and II list the quantitative results.

As shown in Figure 6, fast convergence can be achieved, when the exact solution is smooth and higher-order finite elements are adopted. Particularly, the FEM solution with cubic element can achieve a fairly good consistency with the analytical solution even on coarsest meshes. Hence, it is quite wise to employ elements of higher order than just to refine the meshes further, especially when both of them promise the similar accuracy, as listed in Tables I and II. For BLT forward problem, FEM solution with quadratic element on coarse mesh is able to make a good tradeoff between precision and efficiency.

3.2. *Comparison with MC simulation*

Because of its accuracy and flexibility, MC method has been established as a gold standard for photon propagation simulation in turbid medium. We also performed the numerical experiment to

DOI: 10.1002/cnm

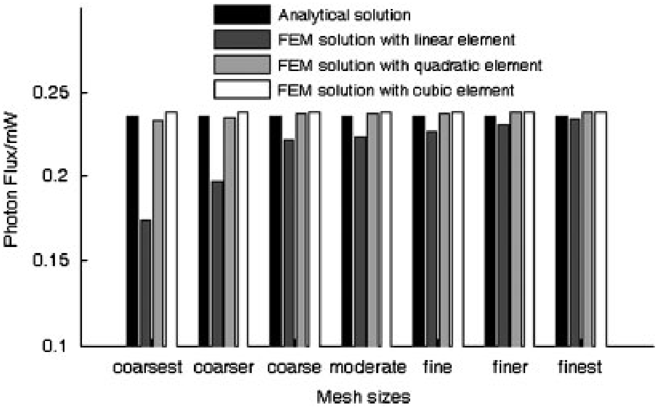

Figure 6. FEM solutions with tetrahedral elements of different orders.

Table I. The quantitative results of FEM solutions with different order elements compared with the analytical solution, which are considered as exact solution and its power is 0.236 mW.

Finite element	Tetrahedra	Degree of freedoms	Relative error	Elapsed time
Linear	226 599	40 214	−0.85%	13.5 s
Quadratic	2124	2058	−0.85%	0.6 s
Cubic	1158	5062	+0.85%	1.2 s

Table II. The convergence orders of FEM solutions with different order elements.

		Linear element		Quadratic element		Cubic element	
Mesh sizes	Tetrahedra	Error norm	Convergence order	Error norm	Convergence order	Error norm	Convergence order
Coarsest	1158	0.062	0.5	0.003	3.6	0.002	4.1
Coarser	2124	0.039	0.8	0.002	3.4	0.002	3.4
Coarse	4456	0.014	1.4	0.001	3.3	0.002	2.8
Moderate	11 070	0.013	1.2	0.001	2.7	0.002	2.3
Fine	20 847	0.009	1.2	0.001	2.4	0.002	2.0
Finer	58 798	0.005	1.3	0.002	1.7	0.002	1.7
Finest	220 001	0.002	1.4	0.002	1.4	0.002	1.4

compare the accuracy between MC and quadratic FEM. A cylindrical phantom of diameter 19 mm and height 30 mm was used. It had the optical parameters of $\mu a = 0.01\,\mathrm{mm}^{-1}$, $\mu s = 3.0\,\mathrm{mm}^{-1}$, $g = 0.80$ and $n = 1.37$. The phantom was discretized into 20 365 tetrahedral elements and 3805 nodes. A total 301 virtual detectors were placed on the phantom surface to record the photon flux density. The phantom was embedded with two light sources, whose parameters were listed in Table III.

Table III. The parameters of light source.

Source no.	Shape	Center (mm)	Diameter (mm)	Height (mm)	Power (nW)
1	Cylinder	(0, 0, 19.9)	0.4	1	170
2	Cylinder	(6, 0, 19.9)	0.4	1	170

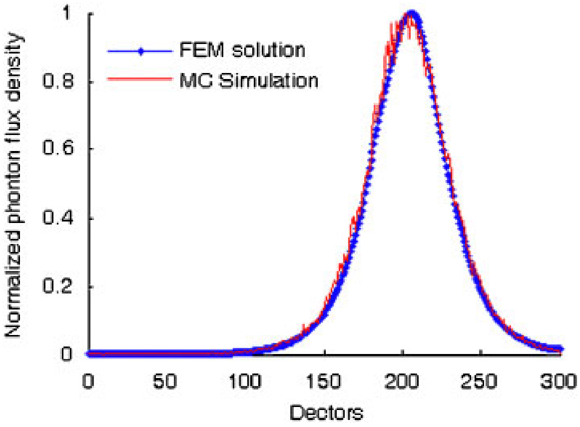

Figure 7. Comparison between FEM solution and MC simulation.

It took about 2 h to perform MC simulation in molecular optical simulation environment [31]. Figure 7 shows that the solution obtained by quadratic FEM is in good agreement with the result from MC simulation with a relative error (RE) of 6.3%. The RE is defined as $\sum_{\text{detectors}} |\Phi_{\text{MC}} - \Phi_{\text{FEM}}| / \sum_{\text{detectors}} \Phi_{\text{MC}}$ [32]. Compared with MC, the quadratic FEM had an excellent computation efficiency that it spent less than 8 s in solving the same problem.

3.3. *Comparison with CCD measurement*

We adopted the same phantom and method to perform the physical experiment, as reported in the literatures [23, 33]. The mouse chest phantom of 30 mm height and 30 mm diameter consisting of four different high molecular polymers to represent muscle (M), lungs (L), heart (H) and bone (B), respectively, as shown in Figure 8(a). Table IV lists the corresponding optical parameters.

The luminescent light stick (Glowproducts, Canada) was selected as the testing light source, which could last for about 4 h at an emission wavelength around 700 nm. Two light tubes were placed inside the two small holes with their centers at $(-9.0, 1.5, 15.0)$ and $(-9.0, -1.5, 15.0)$ in the left lung. Their power were 105.1 and 97.4 nW, respectively. A scientific nitrogen-cooled CCD camera (Roper Scientific Inc, Trenton, NJ) was used for recording the flux density on the cylindrical surface of the phantom, as schematically shown in Figure 8(b).

While obtaining FEM solutions, we had implemented three groups of simulation under different settings. The phantom was discretized into 21 673 linear elements with the coarsest mesh size, 65 529 linear elements with coarse mesh size and 21 422 quadratic elements with the coarsest mesh size, in Simulation 1, 2 and 3, respectively. Figure 9 gives the CCD measurement and the result of Simulation 3. The image in Figure 9(b) was transformed from the flux density on the phantom

DOI: 10.1002/cnm

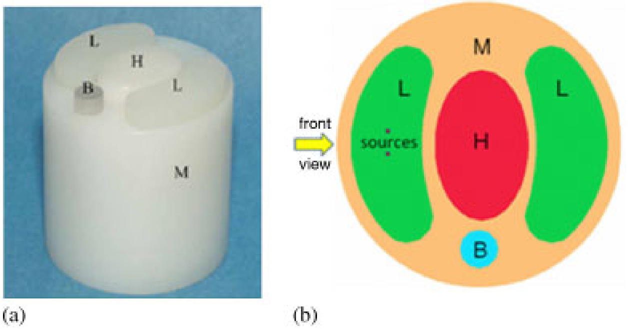

Figure 8. Heterogeneous physical phantom: (a) the phantom consisting of muscle (M), lungs (L), heart (H) and bone (B) and (b) a cross-section through light sources in the left lung. The arrow shows the camera direction during data acquisition.

Table IV. Optical parameters of the physical phantom.

Material	μa (mm^{-1})	μs (mm^{-1})	g	n
Tissue (T)	0.007	10.31	0.90	1.37
Lung (L)	0.023	20.00	0.90	1.00
Heart (H)	0.011	1.96	0.90	1.37
Bone (B)	0.010	3.00	0.98	1.37

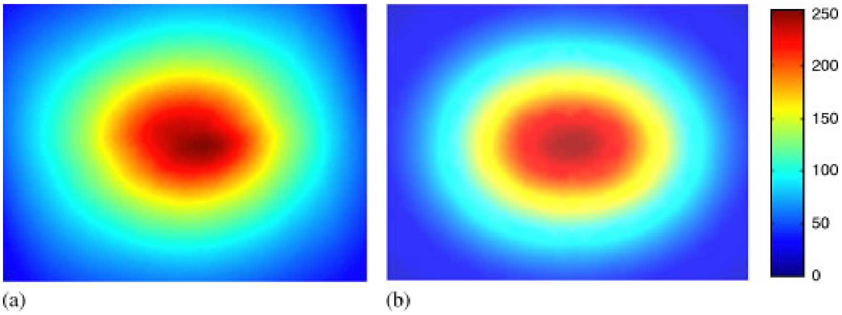

Figure 9. Bioluminescent images of front view: (a) CCD measurement and (b) FEM simulation.

surface by geometric mapping. Both CCD measurement and FEM simulation data were mapped into 24 b bitmap after regularization to simplify the comparison.

We sampled the middle two columns in Figures 9(a) and (b) to make quantitative comparisons, and detailed results are plotted in Figure 10.

As illustrated in Figure 10, simulation 3 with quadratic elements and the coarsest meshes matches CCD measurement best. The mean REs of simulation 1, 2 and 3 are 4.2, 3.2 and 2.8% and the maximum REs are 20.3, 14.3 and 6.8%, respectively. It took 6.9, 15.7 and 12.6 s to perform

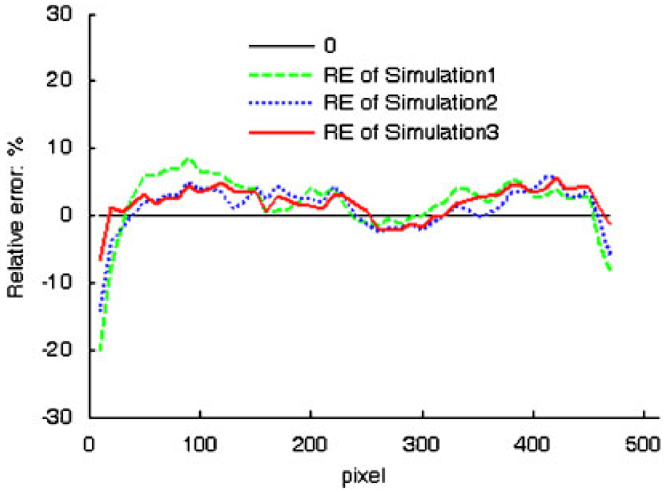

Figure 10. Relative errors (RE) between experimental measurement and three groups of numerical simulation.

simulation 1, 2 and 3. That means simulation 3 based on quadratic elements has the obvious advantages of accuracy and efficiency over simulation 1 and 2, which are based on linear elements.

4. DISCUSSIONS AND CONCLUSIONS

FEM is feasible for the numerical study of BLT forward problem. In this paper, we elucidate the BLT forward problem, introduce the formulation by finite element analysis and discuss FEMs with varying mesh size and varying basis function degree. Both numerical and experimental studies on the accuracy and the convergence of FEM solution are made. As the results indicate, based on proper mesh size and basis function degree, accurate FEM solutions to DE can be obtained efficiently. Moreover, adopting higher-order finite elements will achieve much better accuracy and convergence than just refining the meshes further. For BLT forward problem, quadratic finite elements of coarse size are able to make a good tradeoff between solution accuracy and computation efficiency.

Since the system matrix is sparse and symmetric, specialized techniques on the storage and manipulation for sparse matrix can be employed. When decomposing the geometry into mesh elements, we can only refine ROI (e.g. light source domain), while keeping the remainder intact. Our future work is to focus on the adaptive meshing and multiple sources with complicated tissues. Relevant results will be available later.

ACKNOWLEDGEMENTS

This work is supported by the Chair Professors of Cheung Kong Scholars Programme, the Program for Cheung Kong Scholars, Innovative Research Team in University (PCSIRT, IRT0645), National Basic

DOI: 10.1002/cnm

Research Program of China (NBRPC, 2006CB705700), and Shaanxi Science and Technology Programming (2007K08-06).

REFERENCES

1. Weissleder R, Mahmood U. Molecular imaging. *Radiology* 2001; **219**:316–333.
2. Dzik-Jurasz ASK. Molecular imaging in vivo: an introduction. *British Journal of Radiology* 2003; **76**:S98–S109.
3. Cherry SR. In vivo molecular and genomic imaging: new challenges for imaging physics. *Physics in Medicine and Biology* 2004; **49**:R13–R48.
4. Massoud TF, Gambhir SS. MI in living subjects: seeing fundamental biological process in a new light. *Genes and Development* 2003; **17**(5):545–580.
5. Ntziachristos V, Ripoll J, Wang LV, Weissleder R. Looking and listening to light: the evolution of whole-body photonic imaging. *Nature Biotechnology* 2005; **23**(3):313–320.
6. Wang LV, Wu H. *Biomedical Optics*: *Principles and Imaging*. Wiley: New York, 2007.
7. Wang G, Jiang M, Tian J, Cong W, Li Y, Han W, Kumar D, Qian X, Shen H, Zhou T, Cheng J, Lv Y, Li H, Luo J. Recent development in bioluminescence tomography. *Current Medical Imaging Reviews* 2006; **2**:453–457.
8. Yujie LV, Tian J, Cong W, Wang G, Luo J, Yang W, Li H. A multilevel adaptive finite element algorithm for bioluminescence tomography. *Optics Express* 2006; **14**(18):8211–8223.
9. Cong A, Wang G. Multispectral bioluminescence tomography: methodology and simulation. *International Journal of Biomedical Imaging* 2006; **2006**:1–7. DOI: 10.1155/IJBI/2006/57614.
10. Wang G, Shen H, Kumar D, Qian X, Cong W. The first bioluminescence tomography system for simultaneous acquisition of multi-view and multi-spectral data. *International Journal of Biomedical Imaging* 2006; **2006**:1–8. DOI: 10.1155/IJBI/2006/58601.
11. Lv Y, Tian J, Cong W, Wang G, Yang W, Qin C, Xu M. Spectrally resolved bioluminescence tomography with adaptive finite element analysis: methodology and simulation. *Physics in Medicine Biology* 2007; **52**(15): 4497–4512.
12. Ishimaru A. *Wave Propagation and Scattering in Random Media*. Academic Press: New York, 1978.
13. Li H, Tian J, Zhu F, Cong W, Wang LV, Hoffman EA, Wang G. A mouse optical simulation environment (MOSE) to investigate bioluminescent phenomena in the living mouse with the Monte Carlo method. *Academic Radiology* 2004; **11**(9):1029–1038.
14. Wang LH, Jacques SL, Zheng LQ. MCML-Monte Carlo modeling of photon transport in multi-layered tissues. *Computer Methods and Programs in Biomedicine* 1995; **47**:131–146.
15. Cong WX, Kumar D, Liu Y, Cong A, Wang G. A practical method to determine the light source distribution in bioluminescent imaging. *Proceedings of the SPIE* 2004; **5535**:679–686.
16. Hui L. Studies on forward and inverse problems in in vivo bioluminescent tomography imaging. *Ph.D. Dissertation*, Institute of Automation, Chinese Academy of Sciences, Beijing, 2005.
17. Liu J-L. A finite difference method for symmetric positive differential equation. *Mathematical Computations* 1994; **62**:105–118.
18. Arridge SR, Schweiger M, Hiraoka M, Delpy DT. A finite element approach for modeling photon transport in tissue. *Medical Physics* 1993; **20**:299–309.
19. Schweiger M, Arridge SR, Hiraoka M *et al*. The finite element method for the propagation of light in scattering media: boundary and source condition. *Medical Physics* 1995; **22**:1779–1792.
20. Cong W, Wang G. Boundary integral method for bioluminescence tomography. *Journal of Biomedical Optics* 2006; **11**(2):020503.
21. Song CM, Bazyar MH. Development of a fundamental-solution-less boundary element method for exterior wave problems. *Communications in Numerical Methods in Engineering* 2008; **24**(4):257–279.
22. Arridge SR, Dehghani H, Schweiger M *et al*. The finite element model for the propagation of light in scattering media: a direct method for domains with nonscattering regions. *Medical Physics* 2000; **27**:252–264.
23. Cong W, Wang G, Kumar D, Liu Y, Jiang M, Wang LV, Hoffman EA, McLennan G, McCray PB, Zabner J, Cong A. Practical reconstruction method for bioluminescence tomography. *Optics Express* 2005; **13**:6756–6771.
24. Cong W, Wang LH, Wang G. Formulation of photon diffusion from spherical bioluminescent sources in an infinite homogeneous medium. *Biomedical Engineering*, *Online* 2004; DOI: 10.1186/1475-925X-3-12.
25. Kuzmin D. A high-resolution finite element scheme for convection-dominated transport. *Communications in Numerical Methods in Engineering* 2000; **16**(3):215–223.

26. Lu H, Berzins M, Goodyer CE, Jimack PK. High-order discontinuous Galerkin method for elastohydrodynamic lubrication line contact problems. *Communications in Numerical Methods in Engineering* 2005; **21**(11):643–650.
27. Idelsohn SR, Onate E, Calvo N, Pin FD. The meshless finite element method. *International Journal for Numerical Methods in Engineering* 2003; **58**(6):893–912.
28. Schöberl J, Zaglmayr S. High order Nédélec elements with local complete sequence properties. *COMPEL: The International Journal for Computation and Mathematics in Electrical and Electric Engineering* 2005; **24**(2): 374–384.
29. Lv Y, Tian J, Li H, Luo J, Cong W, Wang G, Kumar D. Modeling the forward problem based on the adaptive FEMs framework in bioluminescene tomography. *Proceedings of SPIE Optics and Photonics*, San Diego, CA, U.S.A., vol. 6318, 2006; 63180I.
30. Demkowicz L, Rachowicz W, Devloo Ph. A fully automatic hp-adaptivity. *Journal of Scientific Computing* 2002; **17**(1–3):127–155.
31. Molecular Optical Simulation Environment. http://www.mosetm.net/.
32. Cong W, Shen H, Cong A, Wang Y, Wang G. Modeling photon propagation in biological tissues using a generalized Delta–Eddington phase function. *Physical Review E* 2007; DOI: 10.1103/PhysRevE.76.051913.
33. Jiang M, Zhou T, Cheng J, Cong W, Wang G. Image reconstruction method for bioluminescence tomography from partial measurement. *Optics Express* 2007; **13**:11095–11116.

DOI: 10.1002/cnm